Received 31 October 2025; revised 15 December 2025; accepted 3 January 2026. Date of publication 12 January 2026; date of current version 26 January 2026.

Digital Object Identifier 10.1109/OJCOMS.2026.3652931

A Correlation-Based Design of RIS for Reduced Power Consumption and Simplified Control Circuitry

ZINA MOHAMED [1] (Member, IEEE), AMMAR B. KOUKI [2] (Senior Member, IEEE), AND SONIA AÏSSA [1] (Fellow, IEEE)

[1] Institut National de la Recherche Scientifique, Montreal, QC H5A 1K6, Canada
[2] École de Technologie Supérieure, Montreal, QC H3C 1K3, Canada

CORRESPONDING AUTHOR: Z. MOHAMED (e-mail: zina.mohamed@inrs.ca)

This work was supported by the Discovery Grant from the Natural Sciences and Engineering Research Council (NSERC) of Canada.

ABSTRACT Aiming at simplifying the hardware structure and reducing the energy consumption in wireless communication via reconfigurable intelligent surfaces (RIS), this paper introduces a novel RIS design founded on the correlation between the phase shift values of the surface elements. First, a correlation analysis is conducted, considering the azimuth angle of a target device within a coverage region spanning from $-80°$ to $80°$. The correlation is demonstrated for different deployment cases, creating the basis for the new RIS structure, termed Connected-RIS, where correlated elements are designed to share the same control signal. The fundamental performance of the proposed design is then analyzed in terms of control signals, power consumption, and communication system performance, comparing it to two RIS structures with full control: one with the same size as in the proposed design, and the other employing the minimum number of elements necessary to satisfy the fair coverage criterion. The correlation-based RIS design enables three-dimensional passive beamforming and significantly reduces the number of required load impedances and control signals, thereby lowering the hardware cost and simplifying the control circuitry. It also achieves substantial power savings as compared to the baseline schemes, while maintaining sufficient gain for a fair radio coverage. For instance, numerical simulations demonstrate that the proposed design reduces the power consumption by almost 86-92% and the control signals by 83-98% compared to operation with fully controlled RIS.

INDEX TERMS Connected RIS, correlation, DC control, energy efficiency, power consumption.

I. INTRODUCTION

THE RIS (reconfigurable intelligent surface) technology is a key enabler for future wireless networks, thanks to its capability to dynamically control the electromagnetic wave propagation [1], [2], [3], [4]. Among multiple ensuing advantages are the improvements in the spectral efficiency, the extensions of the radio coverage, and the reduced power consumptions compared to conventional relaying techniques [5]. Moreover, recent studies on holographic metasurface-based beamforming have demonstrated the growing relevance of advanced intelligent-surface architectures and hardware impairments [6], [7]. With the growing demands for low-power massive connections and green radio in future wireless communications, the reduction of the energy consumption in RIS-assisted communication systems has been gaining increasing research interest [8], [9].

From the architecture viewpoint, conventional RIS structures are typically composed of a number of nearly passive elements, such as tunable meta-atoms, PIN diodes, varactors, and liquid crystals [10]. Although each unit is energy-efficient on its own, the overall hardware complexity and power consumption increase significantly as the surface size increases or that multiple RISs are deployed within the wireless network. Several studies and measurements have shown important findings in this regard. For instance, [11] showed that while a PIN diode only consumes 0.06 mW, the supporting components increase this to 3.7 mW per element. As the number of RIS elements increases, so does the power consumption. In [11], it was shown that a typical 1-bit RIS

of size 27 × 28 consumes an average power of 2.81 W, with micro-controllers using about 160 mW each, and the logic circuit consuming 1.8 W in total. According to [12], deploying ten RIS units, each with 1024 elements, can waste over 35 W of static power just from the control circuits. Also, a 2-bit RIS with 256 elements consumes about 153 W when the total radiated power is 64 W [13], and 33 × 33 elements operating at 5.8 GHz consume approximately 1 W [5]. At high frequencies, where the sizes of unit cells are smaller, the power consumption can be even more significant, e.g., about 200W/m^2 at an operating frequency of 10.6 GHz [11].

While specific prices are not available in the open literature, it is clear that the RIS fabrication cost will be significant, especially when a high number of surface elements are used. Indeed, the more elements a RIS comprises, the higher the number of control signals that are required to configure the surface would be. For instance, an element offering 2^n states requires n bits for the control. With N^2 reflecting elements in a RIS, an equivalent number of control lines would be needed to manage them independently [14]. This scaling can quickly lead to a substantial increase in both the physical wiring and the logical control complexity, as each unit-cell, often implemented with PIN diodes, demands its own dedicated control signal [15], [16], [17].

Beyond the design of the hardware itself, control signaling is a key factor in determining the scalability of RIS. Control architectures can be centralized, where a single controller manages all elements, or distributed, where sub-arrays are independently controlled. Each approach brings trade-offs in scalability, latency, and fault tolerance. To mitigate the substantial overhead for controlling each element individually in large arrays, strategies such as grouping elements and using compact beam index signaling are commonly employed. Recent studies introduced even more efficient control mechanisms. For instance, [16] proposed a quantized codebook that reduces the feedback requirements from linear to logarithmic scaling with the number of RIS elements, making large-scale deployments more feasible. Also, [17] developed a simultaneous information and control signaling protocol, which superimposes the control data onto the user information signals, thereby reducing latency and enabling real-time adaptation.

As the RIS grows in size, the micro-controller or FPGA responsible for generating these signals must also scale, which necessitates additional interface circuitry, hence increasing the overall design cost. To mitigate this, unit-cell grouping can be employed, where multiple elements share common control lines [18], [19], [20], [21]. For instance, [18] proposed a generalized RIS framework, encompassing both stem- and cluster-connected designs, showing that simpler topologies can approach the performance of fully connected RIS. The work in [19] introduced coordinated non-diagonal group-connected RISs, enabling dynamic inter-element routing optimized based on channel state information, while [20] presented the Q-stem connected RIS, which blends single-, tree-, and fully-connected designs to offer scalable complexity. However, they typically rely on predefined or heuristic grouping strategies, without establishing a clear and systematic criterion for connecting RIS elements. Moreover, most existing works are limited to relatively small RIS sizes, which restricts the ability to assess the scalability and performance in deployments with large-aperture RIS. While element grouping reduces the number of required control paths, it also constrains the flexibility to generate complex radiation patterns, leading to an inherent trade-off between the RIS control circuit simplicity and achievable performance.

In addition to these considerations, the high power consumption and the need for sophisticated control mechanisms contribute to the overall cost, making it a critical factor in the widespread adoption of this promising technology. To reduce the implementation cost and optimize the functioning of these intelligent surfaces, it is crucial to design simplified structures for the RIS and its corresponding control circuit. The goal is to enable the implementation of a large aperture while maintaining efficiency and scalability. Indeed, an optimized RIS design is expected to not only minimize the hardware complexity and fabrication cost, but also lower the power consumption, thereby enhancing the overall sustainability of RIS-assisted wireless systems.

Reducing the RIS size and the number of independently controlled elements is crucial for realistic and large-scale deployments. Although RIS elements are nearly passive, practical implementations show that the overall static power and hardware complexity scale unfavorably with the number of elements [14]. Prior measurements demonstrated that supporting circuits can increase the power consumption of a single PIN-diode element from tens of microwatts to several milliwatts, resulting in watt-level consumption for medium-sized panels and tens to hundreds of watts for large surfaces. Moreover, a fully controlled RIS requires one control line per element, which leads to thousands of control connections, a large FPGA/MCU resource demand, and significant wiring overhead. These factors limit the feasibility of deploying large RIS panels on building facades, poles, or indoor infrastructures, particularly in dense networks where multiple RISs may be required. Smaller and structurally simplified RIS architectures therefore provide tangible advantages in terms of installation flexibility, hardware scalability, and energy efficiency. This motivates the need for designs that reduce the number of control signals and active components without compromising the coverage or the beamforming performance. Motivated by these challenges, the proposed design departs from existing grouping approaches by forming connections based on a channel-aware, correlation-driven criterion, enabling hardware reduction without relying on arbitrary or fixed geometric partitions.

This is exactly where this paper's contribution becomes significant, as it consists in advancing an innovative solution that simplifies the RIS architecture while ensuring seamless control and adaptability, ultimately facilitating large-scale deployments of RISs in next-generation wireless networks.

Specifically, the paper proposes a new RIS design founded on the correlation between the phase shift values of the surface elements, a perspective not explored in prior works. In so doing, several contributions are advanced:

- A methodology is proposed for analytically determining the minimum RIS size required to achieve fair coverage, defined by equalizing the power received at the user-equipment (UE) through the RIS-assisted path and the one that would result when the direct communication path between the base station (BS) and the UE exists. The process involves analyzing the received powers, identifying the necessary gain margins, and finding the minimum number of RIS elements essential for effective operation, all while considering realistic 3GPP-based channel models [22].
- The methodology is applied to various deployment scenarios, accounting for the RIS position relative to the BS and the UE, and considering gain margins of 3 dB and 6 dB, thereby providing practical design guidelines for different network configurations.
- For the obtained RIS sizes, phase-shift matrices across steering directions spanning $-80°$ to $80°$ in the azimuth plane are generated. A correlation analysis is then performed to identify RIS elements that exhibit strong phase correlation, thereby quantifying the extent of the target shared control.
- Leveraging the correlation results, we introduce the Connected-RIS, a novel architecture in which correlated elements are grouped to share a single control signal. This design substantially simplifies the control circuitry without compromising the beamforming capabilities.
- The Connected-RIS is thoroughly evaluated in terms of hardware complexity, number of load impedances, number of control signals, power consumption, RIS gain, and achievable data rate. Simulation results demonstrate that the Connected-RIS reduces the power consumption by 86–92% and the number of control signals by 83–98% compared to fully controlled RIS, significantly lowering the implementation cost while maintaining competitive system performance.
- A practical case study is conducted to determine the number of codewords required for full angular coverage. Based on the ensuing results, two deployment strategies are proposed: (i) a dynamically configurable surface with sequential beam steering, and (ii) a static configured surface covering distinct angular sectors. Both strategies are assessed in terms of power efficiency and coverage gain, demonstrating the practical applicability and scalability of the Connected-RIS architecture.

Notations: Vectors and matrices are denoted by lower- and upper-case boldface letters, respectively. The matrix operators $(\cdot)^H$ and $(\cdot)^T$ refer to the Hermitian transpose and transpose, respectively. The symbol $\|.\|$ denotes the Euclidean norm, and $|.|$ is the modulus of a complex number. The mathematical expectation is denoted by $\mathbb{E}[\cdot]$.

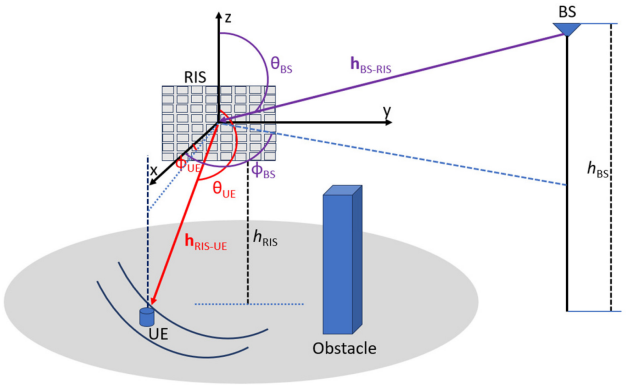

FIGURE 1. Illustration of the RIS-aided downlink communication system.

II. THE RIS-AIDED COMMUNICATION MODEL

We consider a typical RIS-aided wireless communication system model as illustrated in Fig. 1, where a passive RIS, deployed in the $x-z$ plane of the coordinate system shown, is centered at the origin (0,0,0). The RIS consists of a uniform planar array (UPA) of N_y columns and N_z rows. For simplicity, we assume that $N_y = N_z$. The width and the length of each element are denoted by d_y and d_z, respectively. The size of the n^{th} RIS element is hence given by $\mathcal{A}_n = d_y d_z$. The spacing between elements is denoted by δ_1. Let us denote by $\Psi = (\psi_1, \ldots, \psi_{N_y}) \in \mathbb{C}^{N_y \times N_z}$ the matrix of the RIS reflection coefficients, where $\psi_n = [\beta_{n,1} e^{j\phi_{n,1}}, \ldots, \beta_{n,N_z} e^{j\phi_{n,N_z}}] \in \mathbb{C}^{N_z \times 1}$, $\phi_{n,m} \in [0, 2\pi)$ and $\beta_{n,m} \in [0, 1]$, $\forall m \in \{1, \ldots, N_y\}$ and $\forall n \in \{1, \ldots, N_z\}$. Also, let N denote the total number of elements in the RIS.[1]

We assume that the BS, located at a distance $d_{\text{BS,RIS}}$ from the center of the RIS, is characterized by an azimuth angle ϕ_{BS} and an elevation angle θ_{BS}. The single-antenna UE is located at a distance $d_{\text{RIS,UE}}$ from the center of the RIS, and characterized by its azimuth and elevation angles denoted by ϕ_{UE} and θ_{UE}, respectively. The direct line-of-sight (LoS) link between the BS and the UE is assumed to be unavailable due to blockage.

Let $\mathbf{h}_{\text{BS,RIS}} = [h_{\text{BS},1}, \ldots, h_{\text{BS},N}] \in \mathbb{C}^{1 \times N}$ and $\mathbf{h}_{\text{RIS,UE}} = [h_{1,\text{UE}}, \ldots, h_{N,\text{UE}}] \in \mathbb{C}^{N \times 1}$ represent the channel vectors between the BS and the RIS, and between the RIS and the UE, respectively. The propagation channels are modeled by considering the effects of the large-scale fading, represented by $L(d)$, and the small-scale fading, indicated by $\tilde{h}$.[2]

[1]The algorithms and techniques proposed in this work are limited to the passive RIS; however, they can be easily extended to the active RIS case by appropriately modifying the phase-shift matrix to incorporate an amplitude factor $\beta_{n,m} \neq 1$.

[2]This modeling is essential for understanding the performance of the RIS in real-world applications, where factors such as distance, path loss, and fading can significantly influence the signal integrity.

For the large-scale fading, the 3GPP UMi-Street Canyon path loss model [23, Page 26] is used.[3] Hence, we can write

$$L^{\mathrm{dB}}(d) = 32.4 + 21\log_{10}(d) + 20\log_{10}(f), \tag{1}$$

where d is the distance in meters (m), and f is the center frequency normalized by 1 GHz. All distance-related values are normalized by 1 m.

The small-scale fading coefficients follow a Rician distribution [23]. Therefore, the channel coefficients between the BS antenna and the RIS can be expressed as

$$\begin{aligned}\mathbf{h}_{\mathrm{BS,RIS}} &= \sqrt{L\big(d_{\mathrm{BS,RIS}}\big)}\tilde{\mathbf{h}}_{\mathrm{BS,RIS}} \\ &= \sqrt{L\big(d_{\mathrm{BS,RIS}}\big)}\left(\sqrt{\frac{\kappa_{\mathrm{BS,RIS}}}{\kappa_{\mathrm{BS,RIS}}+1}}\mathbf{h}^{\mathrm{L}}_{\mathrm{BS,RIS}} \right. \\ &\qquad \left. + \sqrt{\frac{1}{\kappa_{\mathrm{BS,RIS}}+1}}\mathbf{h}^{\mathrm{NL}}_{\mathrm{BS,RIS}}\right), \end{aligned} \tag{2}$$

where $\kappa_{\mathrm{BS,RIS}}$ is the Rician factor, $L(d_{\mathrm{BS,RIS}})$ is the path loss component in linear scale, with $d_{\mathrm{BS,RIS}}$ being the Euclidean distance between the BS and the RIS, and where $\mathbf{h}^{\mathrm{L}}_{\mathrm{BS,RIS}}$ and $\mathbf{h}^{\mathrm{NL}}_{\mathrm{BS,RIS}}$ respectively denote the deterministic LoS component and the random non-line-of-sight (NLoS) component of the channel from the BS to the RIS. The LoS component is expressed as

$$\mathbf{h}^{\mathrm{L}}_{\mathrm{BS,RIS}} = \left[1, \ldots, \exp\left(\frac{j2\pi\delta_1(N-1)\xi_1}{\lambda}\right)\right], \tag{3}$$

where λ is the carrier wavelength, $\xi_1 = \cos(\theta_{\mathrm{UE}} - \theta_{\mathrm{BS}})\sin(\phi_{\mathrm{UE}} - \phi_{\mathrm{BS}}) + \sin(\theta_{\mathrm{UE}} - \theta_{\mathrm{BS}})$, and δ_1 is the spacing between the RIS elements, set to $\lambda/8$ [24], [25]. For the NLoS component $\mathbf{h}^{\mathrm{NL}}_{\mathrm{BS,RIS}} = [h^{\mathrm{NL}}_{\mathrm{BS},1}, \ldots, h^{\mathrm{NL}}_{\mathrm{BS},N}]$, its entries are modeled as i.i.d. circularly symmetric complex Gaussian random variables with zero mean and unit variance.

Similarly, the channel between the RIS and the UE is expressed as

$$\begin{aligned}\mathbf{h}_{\mathrm{RIS,UE}} &= \sqrt{L\big(d_{\mathrm{RIS,UE}}\big)}\tilde{\mathbf{h}}_{\mathrm{RIS,UE}} \\ &= \sqrt{L\big(d_{\mathrm{RIS,UE}}\big)}\left(\sqrt{\frac{\kappa_{\mathrm{RIS,UE}}}{\kappa_{\mathrm{RIS,UE}}+1}}\mathbf{h}^{\mathrm{L}}_{\mathrm{RIS,UE}} \right. \\ &\qquad \left. + \sqrt{\frac{1}{\kappa_{\mathrm{RIS,UE}}+1}}\mathbf{h}^{\mathrm{NL}}_{\mathrm{RIS,UE}}\right), \end{aligned} \tag{4}$$

where $\kappa_{\mathrm{RIS,UE}}$ is the link's Rician factor, $L(d_{\mathrm{RIS,UE}})$ is the path-loss component, and $d_{\mathrm{RIS,UE}}$ is the Euclidean distance between the RIS and the UE. The LoS component of the channel, i.e., $\mathbf{h}^{\mathrm{L}}_{\mathrm{RIS,UE}}$, is expressed as

$$\mathbf{h}^{\mathrm{L}}_{\mathrm{RIS,UE}} = \left[1, \ldots, \exp\left(\frac{j2\pi\delta_1(N-1)\xi_2}{\lambda}\right)\right], \tag{5}$$

where $\xi_2 = \cos(\theta_{\mathrm{UE}})\sin(\phi_{\mathrm{UE}}) + \sin(\theta_{\mathrm{UE}})$.

[3]This model provides precise predictions for the signal coverage and path loss, making it crucial for network planning and performance evaluation in modern wireless communication systems, including 5G and B5G networks, as it accurately reflects the unique propagation characteristics of dense city centers with tall buildings.

III. COVERAGE DEPENDENCIES ON THE RIS SIZE

A. RIS SIZE FOR FAIR COVERAGE

This section presents a methodology for determining the minimum number of RIS elements needed to ensure fair UE coverage in the communication system described above. Specifically, we examine the RIS size that would be needed to provide the UE with the required service level via the RIS-assisted path, e.g., for users in dead zones or at the cell edge, compared to the case when the UE can be served directly by the BS in case a LoS in between exists.[4] By calculating the required RIS size to make the power received via the RIS-assisted path match or exceed that of a direct BS-UE link, the approach addresses signal disparities and ensures balanced performance for all users regardless of location.

Firstly, let us denote by $h_{\mathrm{BS,\,UE}} \in \mathbb{C}^{1\times 1}$ the channel coefficient between the BS and the UE, given by

$$\begin{aligned}h_{\mathrm{BS,UE}} &= \sqrt{L\big(d_{\mathrm{BS,UE}}\big)}\tilde{h}_{\mathrm{BS,UE}} \\ &= \sqrt{L\big(d_{\mathrm{BS,UE}}\big)}\left(\sqrt{\frac{\kappa_{\mathrm{BS,UE}}}{\kappa_{\mathrm{BS,UE}}+1}}h^{\mathrm{L}}_{\mathrm{BS,UE}} \right. \\ &\qquad \left. + \sqrt{\frac{1}{\kappa_{\mathrm{BS,UE}}+1}}h^{\mathrm{NL}}_{\mathrm{BS,UE}}\right), \end{aligned} \tag{6}$$

where $\kappa_{\mathrm{BS,UE}}$ is the Rician factor of the direct link (BS-UE), $L(d_{\mathrm{BS,UE}})$ is the path-loss component, in which $d_{\mathrm{BS,UE}}$ denotes the Euclidean distance between the BS and the UE, and where $h^{\mathrm{L}}_{\mathrm{BS,UE}}$ and $h^{\mathrm{NL}}_{\mathrm{BS,UE}}$ are the deterministic LoS component and the random NLoS component, respectively.

Next, we outline the methodology for determining the minimum RIS size (number of elements) that is required for the RIS to ensure that the received power via the RIS-assisted path is at least equal to that of the direct path between the BS and the UE in the absence of blockage. This ensures fair coverage for users in dead zones or at cell edges, providing them with signal quality comparable to users with direct LoS connections to the BS.

1) RECEIVED POWER

The UE's received power via the direct path (BS-UE) can be expressed as

$$P^{\mathrm{D}}_{\mathrm{UE}} = P_{\mathrm{t}}L\big(d_{\mathrm{BS,UE}}\big)\left|\tilde{h}_{\mathrm{BS,UE}}\right|^2. \tag{7}$$

The UE's received power from the indirect path (BS-RIS-UE) is given by

$$\begin{aligned}&P^{\mathrm{I}}_{\mathrm{UE}} = \\ &P_{\mathrm{t}}G_{\mathrm{RIS}}L\big(d_{\mathrm{BS,RIS}}\big)L\big(d_{\mathrm{RIS,UE}}\big)\left|\tilde{\mathbf{h}}_{\mathrm{BS,RIS}}\right|^2\left|\tilde{\mathbf{h}}_{\mathrm{RIS,UE}}\right|^2, \end{aligned} \tag{8}$$

where G_{RIS} is the gain of the RIS.

[4]The current framework is evaluated for a single-user scenario for simplicity and tractable analysis. The procedure remains valid for the multi-user case, though additional challenges, such as inter-user interference and resource allocation, would arise, which can be addressed in future work using multi-user beamforming and RIS scheduling strategies

2) FAIR COVERAGE REQUIREMENT

To determine the minimum RIS size that guarantees equal received powers between the RIS-assisted path and the direct path from the BS, we need to consider several factors and establish the fair coverage requirement condition, which can be satisfied by the following equation:

$$P_{\mathrm{UE}}^{\mathrm{I}} \geq P_{\mathrm{UE}}^{\mathrm{D}}. \tag{9}$$

By replacing Eq. (7) and Eq. (8) into Eq. (9), and then rearranging the inequality, the RIS gain satisfying the coverage requirement can be expressed as follows:

$$G_{\mathrm{RIS}} \geq \frac{L\left(d_{\mathrm{BS,UE}}\right)\left|\tilde{h}_{\mathrm{BS,UE}}\right|^2}{L\left(d_{\mathrm{BS,RIS}}\right)L\left(d_{\mathrm{RIS,UE}}\right)\left|\tilde{\mathbf{h}}_{\mathrm{BS,RIS}}\right|^2\left|\tilde{\mathbf{h}}_{\mathrm{RIS,UE}}\right|^2}. \tag{10}$$

To determine the minimum RIS gain in linear scale, denoted by $G_{\mathrm{RIS,\,min}}$, the received power through the cascaded link should be at least equal to the power received through the direct link.

Considering the path loss and small-scale fading, along with the previous inequality, the minimum RIS gain satisfying the fair coverage condition is found, in linear scale, as

$$G_{\mathrm{RIS,\,min}} = \frac{L\left(d_{\mathrm{BS,UE}}\right)\left|\tilde{h}_{\mathrm{BS,UE}}\right|^2}{L\left(d_{\mathrm{BS,RIS}}\right)L\left(d_{\mathrm{RIS,UE}}\right)\left|\tilde{\mathbf{h}}_{\mathrm{BS,RIS}}\right|^2\left|\tilde{\mathbf{h}}_{\mathrm{RIS,UE}}\right|^2}. \tag{11}$$

3) INCORPORATING A GAIN MARGIN

After obtaining the minimum RIS gain satisfying the fair coverage condition and converting it to the dB scale, denoted by $G_{\mathrm{RIS,\,min}}^{\mathrm{dB}}$, a gain margin ΔG^{dB} is added to the latter to obtain the required gain G_{req}. This gain margin serves as a proactive compensation that accounts for the effect of the phrase-shift quantization based on the correlation.[5] Hence, G_{req} can be expressed as

$$G_{\mathrm{req}}^{\mathrm{dB}} = G_{\mathrm{RIS,\,min}}^{\mathrm{dB}} + \Delta G^{\mathrm{dB}}. \tag{12}$$

4) DETERMINING THE REQUIRED RIS SIZE

As the RIS gain is proportional to the total number of elements squared, the gain G_{req}, in linear scale, is proportional to N^2. Therefore, the minimum number of RIS elements that can satisfy this gain can be obtained as follows:

$$N = \sqrt{G_{\mathrm{req}}}. \tag{13}$$

Given the planar structure of the RIS, as described in Section II, we assume that its elements are arranged in a square configuration. Consequently, the total number of elements, N, is distributed as N_{y} and N_{z}, with N_{y} denoting the number of rows and N_{z} denoting the number of columns. The angular coverage will depend on the specific phase-shift matrix used. Operating at frequency f, the half-power beamwidth is approximated as $\theta = \arcsin(\frac{\lambda}{D})$, where $D = N_{\mathrm{z}}\delta_1$. Recall that δ_1 is the element spacing.[6]

B. IMPACT OF THE RIS POSITION

Building upon the methodology established earlier, we now analyze the impact of the RIS position on the minimum RIS size for fair coverage. By applying the derived formula across various deployment cases (cf. Fig. 2), where the RIS is positioned at different locations relative to the BS and the UE, this analysis will reveal the spatial sensitivity of the RIS design and offer practical insights into optimal deployment strategies.

In this study, three deployment cases are considered as illustrated in Fig. 2: 1) *Deployment Case 1*: here, the RIS is positioned near the BS, while satisfying the far-field condition; 2) *Deployment Case 2*: in this case, the RIS is located midway between the BS and the UE; and 3) *Deployment Case 3*: the RIS is assumed to be in close proximity to the UE. Using the law of cosines formula which relates the lengths of the sides of a triangle to the cosine of one of its angles,[7] the distance $d_{\mathrm{RIS,\,UE}}$ is given by $d_{\mathrm{RIS,\,UE}} = \sqrt{d_{\mathrm{BS,\,UE}}^2 + d_{\mathrm{BS,\,RIS}}^2 - 2d_{\mathrm{BS,UE}}d_{\mathrm{BS,RIS}}\cos(\alpha)}$, where the angle α is the angle formed by the links relating the center of the BS to the center of the RIS and the link relating the center of the BS and the user as shown in Fig. 2. Hereafter, by fixing the distances $d_{\mathrm{BS,\,RIS}}$ and $d_{\mathrm{BS,\,UE}}$, the following figures are generated.

Figure 3 illustrates the minimum RIS gain (in dB) as a function of the angle α (in degrees) for the deployment cases described above. The free-space path loss (FSPL), calculated in dB based on $L^{\mathrm{dB}}(d) = 92.45 + 20\log_{10}(d) + 20\log_{10}(f)$, with d being the distance between the transmitter and the receiver in Km and f denoting the carrier frequency in GHz, is used for comparison. Additionally, the Street Canyon and Rician fading models, as described in Section II, and Eqs. (1)–(4), are also considered for benchmarking. As expected, the minimum RIS gain increases as the distance between the BS and the RIS increases, reaching its maximum at $\alpha = 90°$, which is an expected result of the increased path loss. We also observe that the system operating under FSPL conditions consistently requires slightly higher gain compared to operation under Street Canyon conditions at all evaluated distances. The periodic variation of the gain with the angle indicates that the RIS effectiveness depends on its distance w.r.t. the BS and the UE. These results highlight how the RIS performance is affected by both the propagation environment and its position w.r.t. the source and the destination.

[5]Hereafter, ΔG^{dB} is set to 3 or 6 dB. Modeling additional hardware impairments, such as phase noise or non-ideal reflection, is left for future research.

[6]The inter-element spacing is set to $\delta_1 = \lambda/8$, the minimum recommended to limit mutual coupling, representing a worst-case design [26].

[7]This formula is used to find the length of a side when the lengths of the other two sides and the included angle are known.

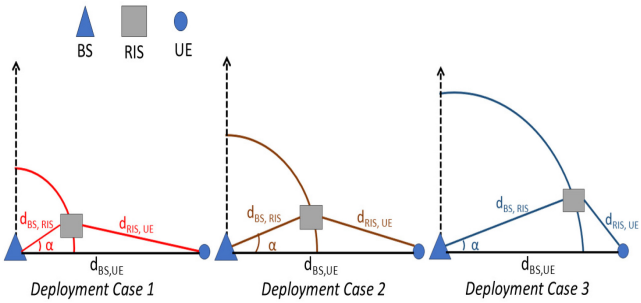

FIGURE 2. Illustration of the deployment cases used to analyze the impact of the RIS position on the minimum RIS size that is required for fair coverage.

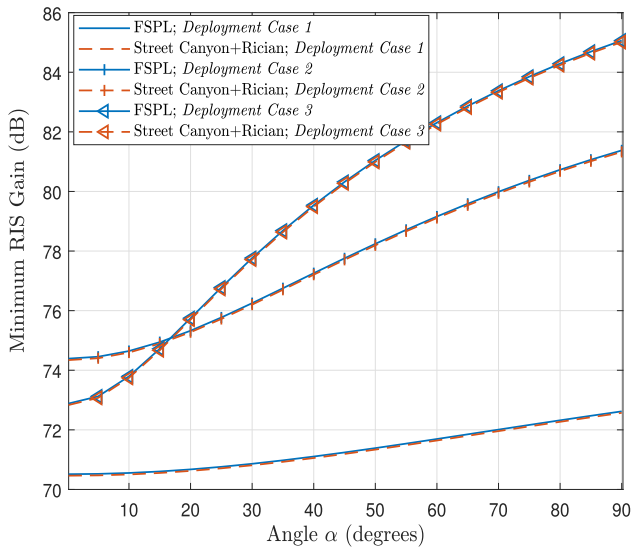

FIGURE 3. The minimum RIS gain versus the angle α.

In Fig. 4, the required number of RIS elements N_z is plotted for the same deployment cases.[8] The plots show how N_z varies with the angle α, factoring in different RIS gain margins and distances between the BS, the RIS, and the UE. As the angle increases, the required number of elements also rises, reflecting an increase in the distance between the RIS and the UE. Lower RIS gain margins, e.g., 3 dB, necessitate less elements compared to higher gain margins, e.g., 6 dB, especially at larger angles. Additionally, as the distance between the RIS and the UE increases, e.g., from 20 m, to 50 m, to 70 m, the number of required elements increases significantly, with sharper growth at higher angles. This demonstrates that the RIS gain margin and the RIS position both play a crucial role in determining the number of required elements to achieve fair coverage.

Considering the system model described in Section II, operating in the mid-band spectrum at 5 GHz, using realistic values for the frequency and the BS's transmit power as specified in [22], next, we apply the methodology to calculate

[8]For clarity of the figure, the curves are plotted as a function of N_z, the number of RIS columns. Since the RIS is square-shaped, the behavior with respect to N_z is representative of that with respect to N_y, i.e., the number of rows, and thus the total number of elements.

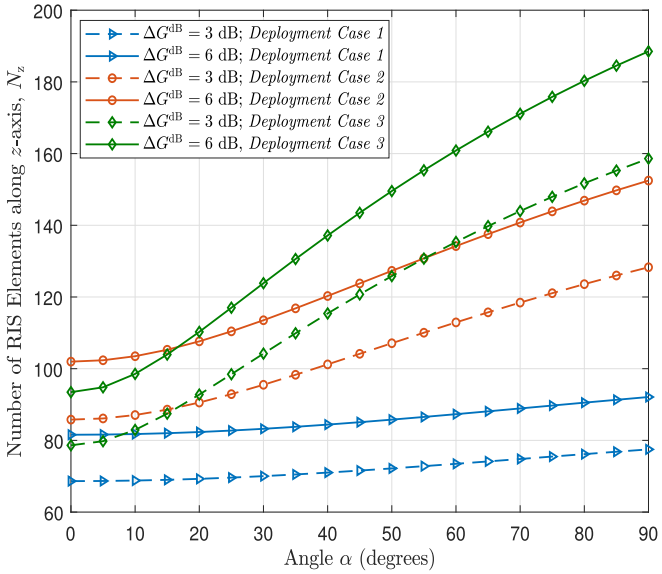

FIGURE 4. The required number of elements along z-axis, N_z. Here, $d_{BS, UE}$ = 100 m.

the minimum number of RIS elements that is required in the deployment cases described above. The system parameters for the three deployment cases are summarized in Table 1. In addition, the Rician factors incorporated in Eqs. (2), (4) and (6) are set as follows: $\kappa^{dB}_{BS,RIS} = 10$ dB, $\kappa^{dB}_{RIS,UE} = 10$ dB, and $\kappa^{dB}_{BS,UE} = 1$ dB.

1) DEPLOYMENT CASE 1

Using the Street Canyon model and the system parameters defined in Table 1, the path losses can be obtained as follows: $L^{dB}d_{BS,\,UE} = 87.07$ dB, $L^{dB}d_{BS,\,RIS} = 72.4$ dB and $L^{dB}d_{RIS,\,UE} = 85.30$ dB. The channel power gain, in linear scale, can be computed using the expression $|h|^2 = 10^{-L^{dB}d/10}(\frac{\kappa}{\kappa+1} + \frac{1}{\kappa+1})$, where $\kappa \in \{\kappa_{BS,RIS}, \kappa_{RIS,UE}, \kappa_{BS,UE}\}$ denotes the Rician factor in linear scale. Using this formula, we obtain the following results: $|\mathbf{h}_{BS,\,RIS}|^2 = 10^{-L^{dB}d_{BS,\,RIS}/10}(\frac{\kappa_{BS,RIS}}{\kappa_{BS,RIS}+1} + \frac{1}{\kappa_{BS,RIS}+1}) = 5.7544\ 10^{-8}$, $|\mathbf{h}_{RIS,\,UE}|^2 = 10^{-L^{dB}d_{RIS,\,UE}/10}(\frac{\kappa_{RIS,UE}}{\kappa_{RIS,UE}+1} + \frac{1}{\kappa_{RIS,UE}+1}) = 2.9512\ 10^{-9}$, and $|h_{BS,\,UE}|^2 = 10^{-L^{dB}d_{RIS,\,UE}/10}(\frac{\kappa_{BS,UE}}{\kappa_{BS,UE}+1} + \frac{1}{\kappa_{BS,UE}+1}) = 1.9596\ 10^{-9}$. Therefore, the minimum RIS gain, based on Eq. (11), is equal to $1.1539\ 10^7$, which is equivalent to 70.625 dB. To achieve this gain, the minimum RIS configuration, referred to as min-gain RIS in this work, consists of 57 × 57 elements.

- *Design Characteristics With 3 dB Gain Margin:* To satisfy a gain margin of 3 dB, the required gain becomes G^{dB}_{req}=73.625 dB. This corresponds to at least $N^2 \geq 4799$ elements, achieved with a square structure of 70 × 70 elements. With an operating frequency of 5 GHz and an inter-element spacing of $\lambda/8 = 0.0075$ m, the RIS edge length is $D = 0.0075 \times 16 = 52.5$ cm, resulting in a surface of size 52.5 cm by

TABLE 1. System parameters and RIS design characteristics for different deployment cases. Here, the surface structure is the conventional fully controlled RIS.

Parameters	*Deployment Case 1*	*Deployment Case 2*	*Deployment Case 3*
$d_{\mathrm{BS,UE}}$ (m)	100	100	100
$d_{\mathrm{BS,RIS}}$ (m)	20	50	70
$d_{\mathrm{RIS,UE}}$ (m)	81.5	55.7	47
$G_{\mathrm{RIS,min}}$ (dB)	70.6250	75.3370	75.6557
Min-Gain RIS Size	57×57	76×76	78×78
$G_{\mathrm{req}}^{\mathrm{3dB}}$ (dB)	73.6250	78.3370	78.6557
3dB-RIS Size	70×70	91×91	93×93
$G_{\mathrm{req}}^{\mathrm{6dB}}$ (dB)	76.6250	81.3370	81.6557
6dB-RIS Size	83×83	108×108	110×110

52.5 cm and a half-power beamwidth of approximately $\theta = 6.5624°$.

- *Design Characteristics With 6 dB Gain Margin:* For a 6 dB margin, the required gain rises to $G_{\mathrm{req}}^{\mathrm{dB}}$=76.625 dB. This can be achieved with a configuration of 83 × 83 elements, giving a surface of size 62.25 cm by 62.25 cm and a beamwidth of $\theta = 5.5319°$.

2) DEPLOYMENT CASE 2

In this case, the minimum RIS gain is $G_{\mathrm{RIS,\,min}} = 75.3370$ dB, corresponding to a min-gain RIS of 76 × 76 elements.

- *Design Characteristics With 3 dB Gain Margin:* When accounting for a 3 dB margin, the gain increases to $G_{\mathrm{req}}^{\mathrm{dB}} = 78.3370$ dB, which necessitates a RIS of 91 × 91 elements. The size becomes 68.25 cm by 68.25 cm, and the beamwidth is approximately $\theta = 5.04°$.
- *Design Characteristics With 6 dB Gain Margin:* In this setup, the required gain is $G_{\mathrm{req}}^{\mathrm{dB}} = 81.3370$ dB, met with 108 × 108 elements, which results in a RIS size of 81 cm by 81 cm and a narrower beamwidth of $\theta = 4.2399°$.

3) DEPLOYMENT CASE 3

In this case, the required gain is $G_{\mathrm{RIS,\,min}} = 75.6557$ dB, leading to a min-gain RIS of 78 × 78 elements.

- *Design Characteristics With 3 dB Gain Margin:* By adding a 3 dB margin, the required gain is $G_{\mathrm{req}}^{\mathrm{dB}} = 78.6557$ dB, satisfied with a square RIS of 93 × 93 elements. The resulting size is 69.75 cm by 69.75 cm, and the beamwidth is approximately 4.9274°.
- *Design Characteristics With 6 dB Gain Margin:* For a 6 dB margin, a gain of 81.6557 dB is required, corresponding to a configuration of 110 × 110 elements. The RIS in this case spans 82.5 cm by 82.50 cm and has a beamwidth of about 4.1826°.

IV. THE CONNECTED-RIS DESIGN

The proposed correlation-based approach is general and can be applied to variations in both azimuth and elevation steering directions. However, for clarity and to isolate the dominant effects observed in typical urban deployments, we restrict our analysis to variations in the azimuth direction. Accordingly, we assume fixed values for θ_{BS}, ϕ_{BS}, and θ_{UE}, and vary only the UE position through the azimuth angle ϕ_{UE}.[9] Ideal CSI at the RIS and the BS is assumed, which can be obtained using channel estimation techniques such as parallel factor decomposition [29].[10] For each UE position defined by the steering direction ϕ_{UE}, the phase-shift matrix Ψ is constructed using the following expression [30]:

$$\psi_{n,m} = \exp\big(-j\big(\angle h_{\mathrm{BS},n,m} + \angle h_{n,m,\mathrm{UE}}\big)\big), \quad \forall n \in \{1,\ldots,N_{\mathrm{z}}\}\ \forall m \in \{1,\ldots,N_{\mathrm{y}}\}. \tag{14}$$

The objective is to cover the region defined by the azimuth angle ϕ_{UE} spanning from $-80°$ to $80°$, and generate the phase-shift matrix for each steering direction ϕ_{UE}. To achieve this, we adopt the procedure described in Algorithm 1. The process is repeated for each of the three deployment cases described in Section III-B.

The results in Fig. 5 illustrate the RIS gain as a function of the azimuth angle $\phi \in [-80°, 80°]$ for a steering direction $\phi_{\mathrm{UE}} = -80°$, along with the corresponding minimum gain in this configuration. It is observed that the RIS gain attains its minimum value, namely, $G_{\mathrm{RIS,min}} = 70.625$ dB, at approximately $\phi_q = -76°$. This angle is then used to compute the subsequent steering direction, as outlined in Algorithm 1. The same procedure is iteratively applied to determine the successive angle ϕ_{q+1} and the associated phase-shift matrix Ψ_{q+1}, as described in Algorithm 1, continuing until the steering direction reaches $\phi_{\mathrm{UE}} = 80°$.

A. CORRELATION ANALYSIS

We now outline the method to design the new RIS based on correlation. The process for identifying correlated elements consists in the following steps:

- **Selecting Element Pairs:** Computing the phase-shift differences between all possible pairs of entries in matrix Ψ_q, and storing the results in the vector

[9] In urban settings, RIS coverage is primarily constrained in the horizontal plane due to obstacles such as buildings, whereas elevation variations are usually negligible because building heights and RIS placements often lead to an approximately constant elevation angle for ground-level UEs [27], [28].

[10] While practical CSI is affected by estimation errors and delays, the proposed framework serves as a performance benchmark, and the qualitative behaviors are expected to remain consistent with only minor degradation.

Algorithm 1 RIS Phase-shift Design and Beam Steering.

Input: N, $\phi_{\text{BS}}, \theta_{\text{BS}}$, θ_{UE}, $d_{\text{BS,RIS}}$ $d_{\text{RIS,UE}}$.

Initialize $\phi_{\text{UE}} = -80°$.
Generate the channel dataset using (6) and (4).
Compute the initial phase-shift matrix Ψ_1 at ϕ_{UE} using (14).
Evaluate the RIS gain $G_{\text{RIS}}(\phi)$ for $\phi \in [-80°{:}1°{:}80°]$.
Find the angle $\phi_{\min}$ such that $G_{\text{RIS}}(\phi_{\min}) = G_{\text{RIS,min}}$.
Set the iteration index $q = 1$.
while $\phi_q \leq 80°$ **do**
  Generate the channel dataset using (6) and (4).
  Compute the phase-shift matrix Ψ_q using (14) at ϕ_q.
  Evaluate the RIS gain $G_{\text{RIS}}(\phi)$ for $\phi \in [-80°{:}1°{:}80°]$.
  Identify ϕ_q where $G_{\text{RIS}}(\phi_q) = G_{\text{RIS,min}}$.
  Compute the phase difference: $\Delta\phi = \phi_q - \phi_{q-1}$.
  Update the steering angle: $\phi_{q+1} = \phi_q + \frac{\Delta\phi}{2}$
  Compute the next phase-shift matrix Ψ_{q+1}
  Increment the iteration index: $q \leftarrow q + 1$
end while
Set $Q = q - 1$.

Output: Phase-shift matrices $\{\Psi_q\}_{q=1}^{Q}$.

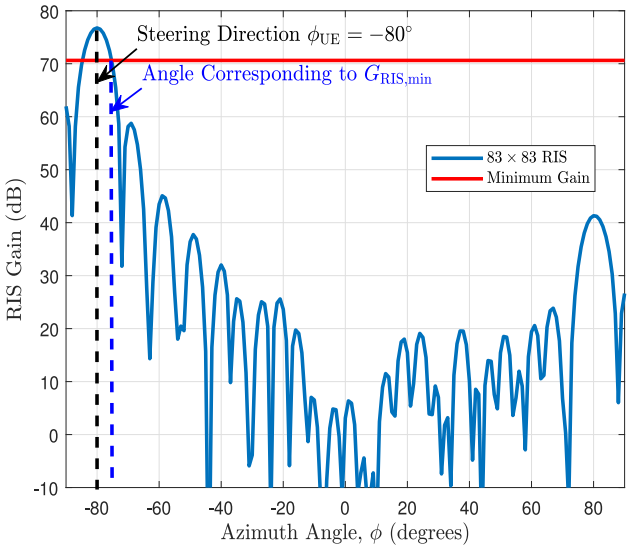

FIGURE 5. RIS gain versus azimuth angle ϕ for a steering direction $\phi_{\text{UE}} = -80°$ in *Deployment Case 1*, i.e., RIS near the BS. Here, $\Delta G^{\text{dB}} = 6$ dB.

$\Delta\Psi_q$. This process is repeated for all phase-shift matrices $\{\Psi_q\}_{q=1}^{Q}$ generated using Algorithm 1, and the corresponding differences are stored in the vectors $\{\Delta\Psi_q\}_{q=1}^{Q}$.

- **Defining the Correlation Threshold:** A predefined threshold, ψ_{th}, determines whether two elements are correlated. The threshold is set based on the desired correlation level and the specific requirements of the deployment scenario.
- **Quantifying Correlation:** To capture the correlation state of each element, we use a binary variable, $b_m \in \{0, 1\}$ for $m \in \{1, 2, \ldots, M\}$, where $M = \binom{N^2}{2}$ is the total number of element pairs. If the phase-shift difference between a pair of elements $\Delta\Psi_{m,q}$, $q \in \{1, \ldots, Q\}$, is less or equal to the predefined threshold across all the scenarios, the elements are considered as correlated and b_m is set to unity; otherwise $b_m = 0$.

Algorithm 2 Correlation Analysis.

Input: Ψ_q, $\forall q \in \{1, \cdots, Q\}$; ψ_{th}.

Initialize $M = \binom{N^2}{2}$, $\mathbf{b} = \mathbf{0}_{M\times 1}$, $\Delta\Psi_q = \mathbf{0}_{M\times 1}$, and $\mathbf{K}_{\text{pairs}} = \mathbf{0}_{M\times 4}$, for storing the binary decisions, the phase-shift differences, and the index pairs, respectively.
for $q \in \{1, \cdots, Q\}$ **do**
  for each element pair (i, j) in Ψ_q **do**
    Compute the difference $\Delta\Psi_q[m] \leftarrow \Psi_q[i] - \Psi_q[j]$.
  end for
end for
for $m \in \{1, \cdots, M\}$ **do**
  if $\Delta\Psi_q[m] \leq \psi_{\text{th}}$ for all $q \in \{1, \ldots, Q\}$ **then**
    $b[m] \leftarrow 1$.
    Extract the corresponding indexes (i, j).
    Store indexes in $\mathbf{K}_{\text{pairs}}[m]$.
  else
    $b[m] \leftarrow 0$.
  end if
end for
Store $\mathbf{K}_{\text{pairs}}$ and $\mathbf{b}$ in a final matrix $\mathbf{F} = [\mathbf{K}_{\text{pairs}}\mathbf{b}]$.

Output: Matrix $\mathbf{F}$ containing the index pairs and the binary decisions.

The binary values are stored in a vector $\mathbf{b} = [b_1, b_2, \ldots, b_M]$, which represents the correlation among the M pairs of phase shifting elements. If the correlation vector contains only ones, the RIS is deemed as fully connected. When $b_m = 1$, the two elements corresponding to the m^{th} combination are correlated and can be connected together.

Algorithm 2 summarizes the correlation analysis process, detailing the steps for generating the phase-shift matrices, computing the phase differences, and identifying the correlated elements. The correlation process is conducted for each of the three deployment cases described in Section III-B. The proposed correlation-based grouping principle is general and remains applicable to other RIS technologies, including active RIS and hybrid RIS, making the framework broadly relevant to future intelligent surface designs.

Since the threshold value ψ_{th} directly impacts the number of correlated elements, next we analyze this relationship. An exhaustive search is adopted to obtain the optimal threshold value. Specifically, at each iteration, the threshold is increased by 1° and the number of correlated elements is evaluated. The search is stopped once the maximum number of correlated elements is achieved, and the corresponding threshold value is selected as optimal.

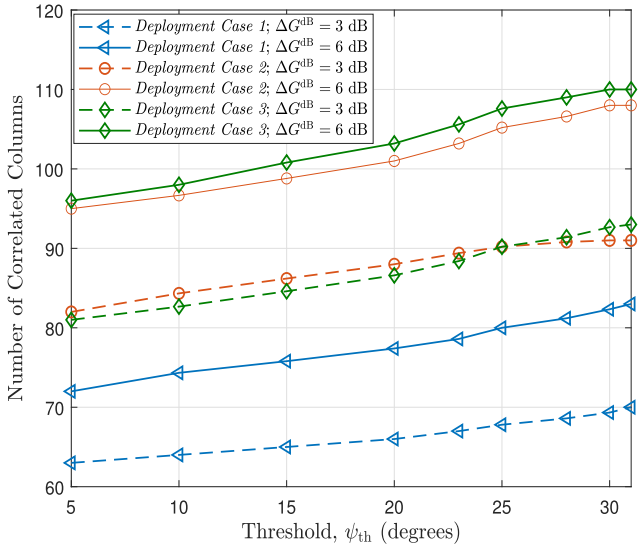

FIGURE 6. Number of correlated columns versus the threshold value ψ_{th}.

Figure 6 illustrates the relationship between the number of correlated columns and the threshold value ψ_{th} for the three deployment cases described in Section III-B. For instance, in deployment case 1, where the RIS is near the BS, the maximum number of correlated elements occurs at $\psi_{\text{th}} = 31°$ for $\Delta G^{\text{dB}} = 3$ and at $\psi_{\text{th}} = 30°$ for $\Delta G^{\text{dB}} = 6$, indicating optimal threshold values for these configurations. At lower threshold values, such as $\psi_{\text{th}} = 15°$, all scenarios exhibit a notably reduced number of correlated columns. This suggests that increasing ψ_{th} enhances the correlation among the columns. Furthermore, the variation in the correlation trends across the three cases underscores the significant impact of the deployment configuration on the nature of the correlation.

Figure 7(I) illustrates the correlation patterns obtained with the threshold $\psi_{\text{th}} = 15°$ for the deployment scenarios discussed above. The results show that the correlation does not span all RIS columns uniformly. Instead, only specific clusters of adjacent elements exhibit sufficiently similar phase responses to be grouped, while others remain weakly correlated and must therefore be treated as independent. It also highlights that, under a relatively low threshold such as $\psi_{\text{th}} = 15°$, many columns cannot be merged. Such a design is particularly suitable for scenarios requiring support for multiple users or the simultaneous generation of multiple independent beams.

Figure 7(II) shows the results obtained by applying the proposed methods (Algorithm 1 and Algorithm 2) for the three deployment cases under consideration. The threshold values used are respectively $\psi_{\text{th}} = 30°$ and 31°, 24° and 29°, 31° and 28°. The figure demonstrates a strong correlation along the columns of the RIS, suggesting that the elements within each column can be grouped together and controlled using a single control signal. This implies that, for effective beamforming in the desired direction, it is sufficient to configure the phase shifts of the elements in the first row of the RIS and the remaining elements within the same column are obtained by adding the threshold value ψ_{th} (cf. Fig. 8). This leads to the proposed RIS structure, namely, the Connected-RIS. This structure ensures that the imposed phase pattern propagates consistently across the remaining elements in each column of the surface.

Figure 8 illustrates the RIS circuitry and control architecture. It shows individual RIS elements, the grouping of correlated elements, and how a single control line drives each group. The figure emphasizes the reduction in both load impedances and DC control lines compared to a fully controlled RIS. Arrows and annotations highlight how correlated elements share the same control signal, simplifying the circuitry while maintaining full beamforming capability.

B. COMPLEXITY ANALYSIS

The computational complexity of the proposed algorithms is largely dominated by the correlation analysis. For a RIS of size $N = N_{\text{z}} \times N_{\text{y}}$ with Q steering directions, generating the phase-shift matrices Ψ_q for each steering direction requires $\mathcal{O}(NQ)$ operations, scaling linearly with the number of elements and steering directions. The correlation analysis, which evaluates the maximum pairwise phase differences between columns of the phase-shift matrices, has a worst-case complexity of $\mathcal{O}(N^2 N_{\text{z}} Q)$. In practice, early-stopping mechanisms can significantly reduce the number of comparisons when columns are found to be uncorrelated, improving the average-case efficiency. Finally, grouping correlated columns to form the Connected-RIS control groups involves a simple linear scan over N_{y} columns, i.e., $\mathcal{O}(N_{\text{y}})$, which is negligible compared to the correlation step.[11]

V. PERFORMANCE EVALUATION OF THE CONNECTED-RIS

A. CONTROL AND LOAD IMPEDANCE

In the Connected-RIS architecture, the first element of each column is a reconfigurable unit modeled by a load impedance Z_i, where $i \in \{1, \ldots, N_{\text{z}}\}$. Here, N_{z} denotes the number of groups of correlated elements, which corresponds to the number of columns in the structure. For comparison purposes, two benchmark designs are considered, both based on fully controlled elements: (i) the min-gain RIS, which corresponds to the RIS structure with the minimum number of elements that satisfies the fair coverage criterion (cf. Section III); and (ii) the ΔG^{dB}-RIS, which refers to the conventional RIS where the number of elements is selected to achieve the required gain after adding a gain margin $\Delta G^{\text{dB}} = 3\text{dB}$ or 6dB.

[11] A detailed hardware-level analysis, including memory usage and FPGA resource consumption, is beyond the scope of this work. Nevertheless, the Connected-RIS reduces the number of controlled elements from N^2 (fully controlled RIS) to N_{z} groups, implying a proportional reduction in memory and FPGA utilization by approximately a factor of N/N_{z} [31], [32].

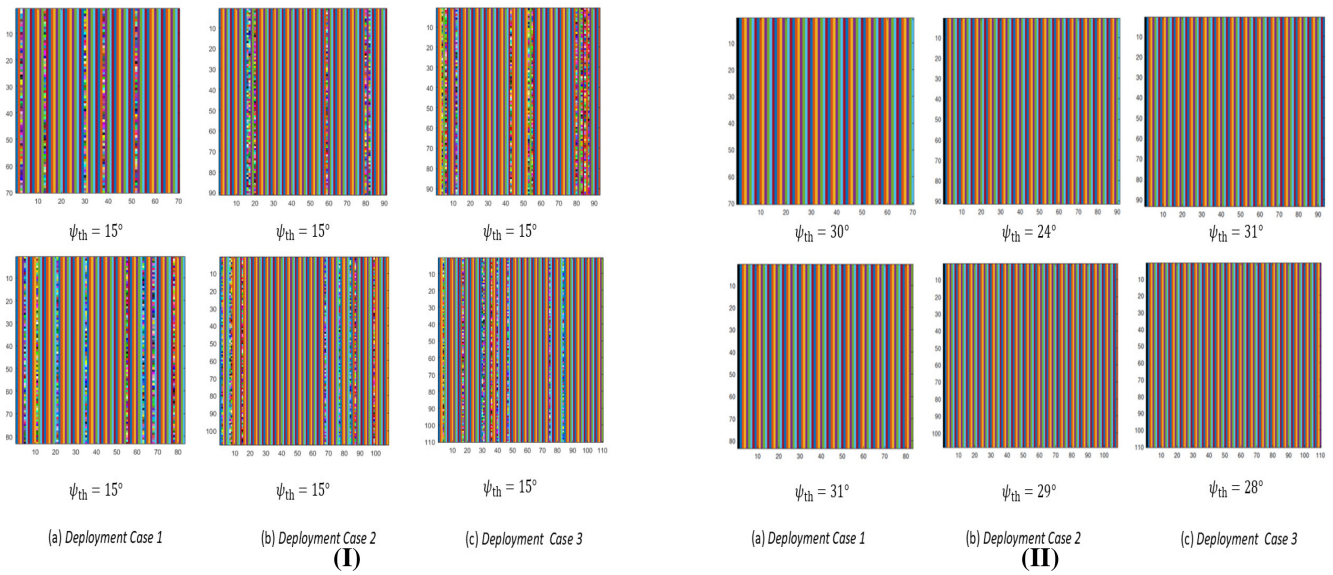

FIGURE 7. Illustration of correlated elements in the three deployment cases: RIS elements sharing the same color maintain the same phase-shift difference as the steering direction ϕ_{UE} varies from $-80°$ to $80°$. (I) $\psi_{th} = 15°$; and (II) optimal threshold values. In both sub-figures, the first row corresponds to $\Delta G^{dB} = 3$ dB and the second row corresponds to $\Delta G^{dB} = 6$ dB.

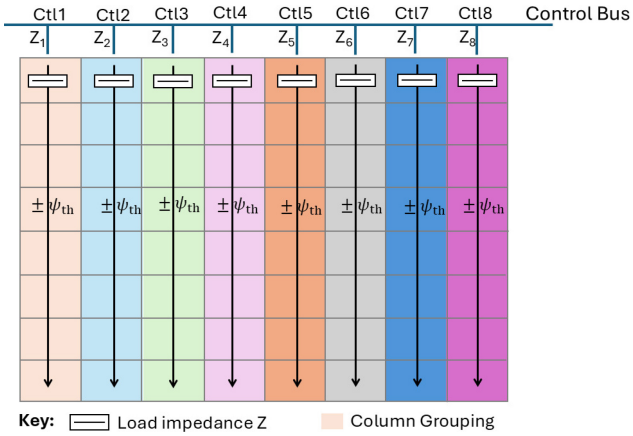

FIGURE 8. An 8 × 8 illustration of the Connected-RIS circuitry with column-wise grouping, a single load impedance per column placed on the top element, and the phase propagation to the remaining elements indicated by ψ_{th}.

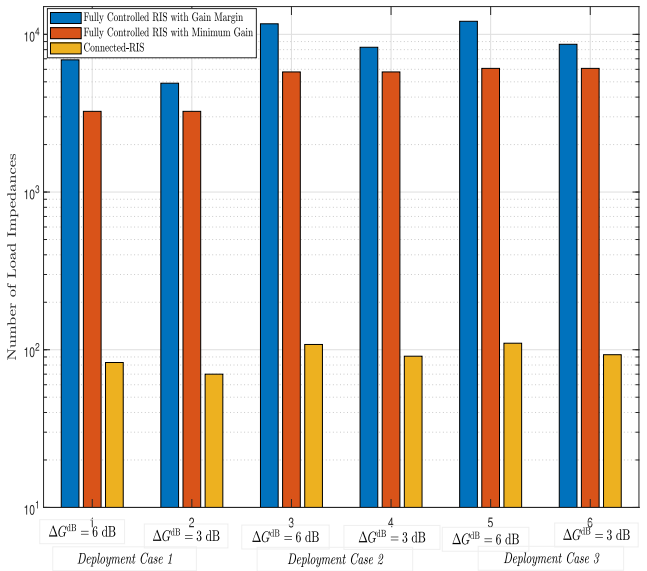

FIGURE 9. Number of load impedances: comparison of Connected-RIS versus two benchmarks in different deployment cases.

Figure 9 illustrates that the Connected-RIS architecture significantly reduces the number of required load impedances compared to the fully controlled RIS structures (3dB-RIS or 6dB-RIS, and the min-gain RIS) across all the deployment cases. This reduction is consistently observed for both margins, i.e., $\Delta G^{dB} = 6$ dB and $\Delta G^{dB} = 3$ dB, with the Connected-RIS exhibiting an exponential decrease in impedance requirements, as evidenced by the logarithmic scale. This substantial reduction leads to lower hardware complexity, reduced implementation costs, and a more simplified design of the DC control circuitry, thereby positioning the Connected-RIS as a more efficient and scalable architecture.

For the proposed Connected-RIS design, we introduce a DC control circuit, where each load impedance is driven by a single DC bias control line, with a shared ground connection used as the return path. In total, the Connected-RIS requires 83 DC control lines, compared to 6889 control lines for the fully controlled 6dB-RIS, and 70 DC biasing instead of 4900 control lines required for the fully controlled 3dB-RIS. In both configurations, the Connected-RIS also outperforms the fully controlled with minimum gain RIS, which requires 3249 control lines. This substantial reduction in the number of control lines highlights the markedly lower complexity of the DC control circuit in the Connected-RIS design, making it a more practical and scalable alternative to the fully controlled RIS architectures.

A further comparison in terms of the number of BS-RIS control signals can also be considered. We find that the number of control signals transmitted from the BS to the RIS via the separated control link is N^2 for the fully controlled RIS (3dB-RIS, 6dB-RIS, and min-gain RIS), where N is the total number of RIS elements ($N = N_{\text{req}}$ or $N = N_{\text{min}}$ according to the structure); and N_{z}^2 for the Connected-RIS, with N_{z} is the number of correlated elements (columns), which is always less than that of the fully controlled RIS structures.

B. POWER CONSUMPTION ANALYSIS

Now, we evaluate the power consumption of the proposed architecture. The power consumption of a RIS can be divided into two main components: the static power and the unit cell power [31]. The static power, denoted P_{static}, corresponds to the power required by the control board and drives the circuits, e.g., registers. Power P_{units} represents the power consumed by the RIS unit cells, which varies depending on the type of switching elements used. Based on this description, the power consumption of the RIS can be expressed as

$$P_{\sum} = P_{\text{static}} + P_{\text{units}}, \tag{15}$$

where $P_{\text{static}} = P_{\text{control}} + P_{\text{circuit}}$, in which P_{control} is the power consumption of the control board, which can be considered as constant, and P_{circuit} is the power consumption of the drive circuits. The latter depends on the type of adjustable electronic components, the number of control signals, and the self-power consumption characteristics [32]. Based on that, P_{circuit} of the Connected-RIS can be formulated as

$$P_{\text{circuit}} = \left\lceil \frac{N_{\text{c}}}{N_{\text{z}} N_{\text{s}}} \right\rceil P_{\text{drive}}, \tag{16}$$

where N_{c} is the number of adjustable electronic components, N_{s} is the number of control signals, N_{z} is the number of correlated elements, which corresponds to the number of columns of the RIS, $\lceil \cdot \rceil$ is the ceiling function, and P_{drive} is the power consumption of the drive circuit, which depends on the bit resolution of the reflecting elements.

For comparison purposes, we also provide the expression for the circuit power consumption corresponding to the fully controlled RIS (with gain margin and with minimum gain), which is given by

$$P_{\text{circuit}} = \left\lceil \frac{N_{\text{c}}}{N N_{\text{s}}} \right\rceil P_{\text{drive}}. \tag{17}$$

Let P_{unit} denote the power consumption of a reflecting element along with the supporting biasing circuit (unit cell). In this case, the reflecting element consists of three PIN diodes, with the PIN diode's individual power denoted by P_{diode}. Therefore, the total power of each unit cell is given by $P_{\text{unit}} = 3P_{\text{diode}}$. Hence, the total power of the RIS units is obtained as $P_{\text{units}} = N_{\text{units}} P_{\text{unit}}$, where

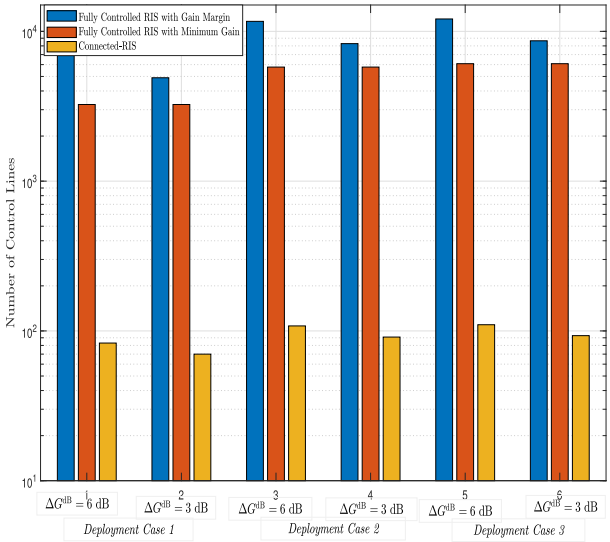

FIGURE 10. Number of control lines: comparison of Connected-RIS versus two benchmarks in different deployment cases.

N_{units} is the total number of elements. In this work, we define the number of units as either $N_{\text{units}} = N$, for the fully controlled RIS or $N_{\text{units}} = N_{\text{z}} = N_{\text{y}}$ for the Connected-RIS.

The FPGA XC7K70T is embedded as the control board, with a working voltage of 24 V and a current of 0.2 A [31]. Hence, $P_{\text{control}} = P_{\text{FPGA}} = 4.8$ W. We assume that the power consumption of a RIS unit is $P_{\text{unit}} = 15$ mW. Here, we employ a 4-bit shift register, which typically consists of three D flip-flops connected in series to control each element (TTL 74LS194), thus $P_{\text{drive}} = 75$ mW. Based on these values, the total power consumption of a RIS panel in the three design configurations, namely, the fully controlled RIS with gain margin (the 3dB-RIS, the 6dB-RIS), the fully controlled RIS with minimum gain (the min-gain RIS), and the Connected-RIS, is compared in Table 2 for the three deployment cases described in Section III-B.

A key finding from Table 2 is that the Connected-RIS structure, designed based on the correlation analysis, offers substantial power savings compared to the fully controlled structures (3dB-RIS, 6dB-RIS, and the min-gain RIS). For example, in *Deployment Case 1*, the Connected-RIS consumes only 5.86 W, whereas the 3dB-RIS and the min-gain RIS consume 78.41 W and 43.82 W, respectively. This corresponds to a power reduction of approximately 92.5% relative to the 3dB-RIS architecture, and 86.6% relative to the min-gain one. Moreover, the Connected-RIS exhibits robustness to gain margin variations, with only a minor increase in the power consumption when the gain margin is increased from 3 dB to 6 dB, unlike the fully controlled RIS, which experiences a significant rise. For all deployment cases, the proposed RIS architecture consistently maintains low power consumption, even as the distance of the RIS from the BS increases, demonstrating its scalability and adaptability.

TABLE 2. RIS power consumption for different deployment cases.

RIS Power Consumption (W)					
Deployment Cases	**Connected-RIS (3 dB)**	**Connected-RIS (6 dB)**	**3dB-RIS**	**6dB-RIS**	**Min-Gain RIS**
Case 1	5.860	6.045	78.410	108.240	43.815
Case 2	6.170	6.420	129.127	179.87	91.440
Case 3	6.200	6.450	134.647	186.412	96.060

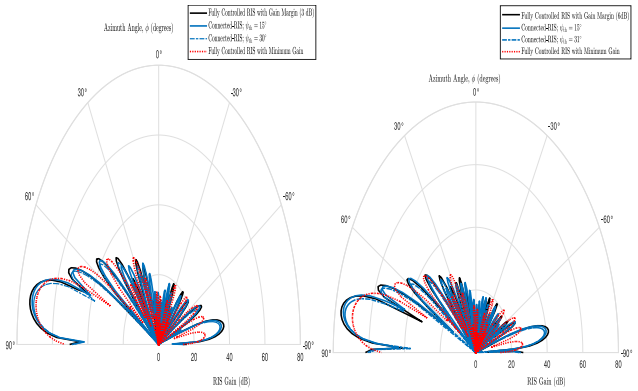

FIGURE 11. RIS gain versus azimuth angle ϕ in *Deployment Case 1*, with $\phi_{\text{UE}} = 80°$: (a) $\Delta G^{\text{dB}} = 3$ dB, (b) $\Delta G^{\text{dB}} = 6$ dB.

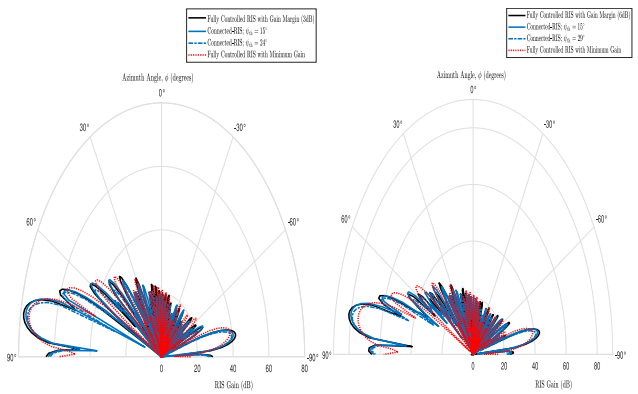

FIGURE 12. RIS gain versus azimuth angle ϕ in *Deployment Case 2*, with $\phi_{\text{UE}} = 80°$: (a) $\Delta G^{\text{dB}} = 3$ dB, (b) $\Delta G^{\text{dB}} = 6$ dB.

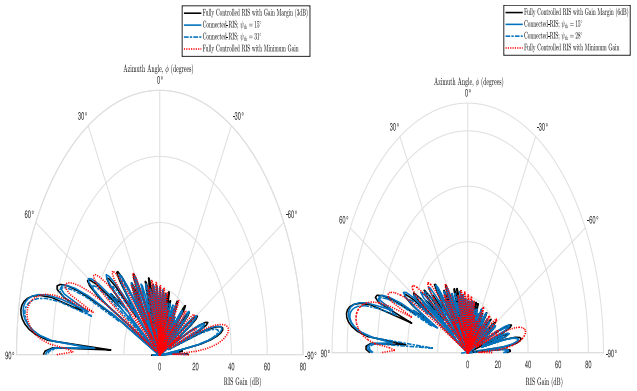

FIGURE 13. RIS gain versus azimuth angle ϕ in *Deployment Case 3*, with $\phi_{\text{UE}} = 80°$: (a) $\Delta G^{\text{dB}} = 3$ dB, (b) $\Delta G^{\text{dB}} = 6$ dB.

C. GAIN ANALYSIS

Now, we conduct a performance evaluation of the RIS gain achieved by the Connected-RIS design, in comparison with the fully controlled designs.

Figures 11–13 present a comprehensive evaluation of the RIS gain performance across various configurations: the fully controlled RIS with gain margin, the fully controlled RIS with minimum gain, and the Connected-RIS, in the deployment cases described in Section III-B, considering different threshold values ψ_{th}. For instance, as shown in Fig. 12, the fully controlled and the Connected-RIS exhibit similar gain characteristics, with minor angular shifts in the Connected-RIS nulls. Although the maximum gain of the Connected-RIS remains slightly below that of the fully controlled RIS with gain margin, it continues to exceed the performance of the fully controlled RIS with minimum gain, thereby ensuring compliance with fair coverage requirements. While the fully controlled RIS with gain margin offers high performance, its excessive power consumption renders it unsuitable for large-scale deployments (cf. Table 2). Although the fully controlled RIS with minimum gain is more efficient than that with gain margin (ΔG^{dB}-RIS) configurations, it remains less energy-efficient than the Connected-RIS. These results underscore the Connected-RIS as a compelling architecture for next-generation wireless networks, offering a favorable trade-off between performance and energy efficiency, particularly in energy-constrained and large-scale scenarios. Overall, the Connected-RIS demonstrates a strong ability to balance the control complexity with the system performance, and to reliably meet the fair coverage condition in diverse deployment conditions.

D. RATE ANALYSIS

While reducing power consumption is essential for enhancing the energy efficiency, it is equally important to ensure that this improvement does not compromise the communication rates or the overall system performance. Therefore, evaluating the achievable rate is crucial for determining whether the Connected-RIS design maintains an acceptable trade-off between the energy efficiency and the communication effectiveness. In these investigations, we set $N_0 = -174 + 10\log_{10}(B)$ dBm, where $B = 1$ MHz is the system bandwidth [12].

In Figs. 14 and 15, the achieved rate at the typical UE is plotted for the Connected RIS, and the fully controlled RIS configurations. The results reveal that all configurations attain nearly identical rates. This outcome can be attributed to the fact that the three RIS structures are designed to optimize

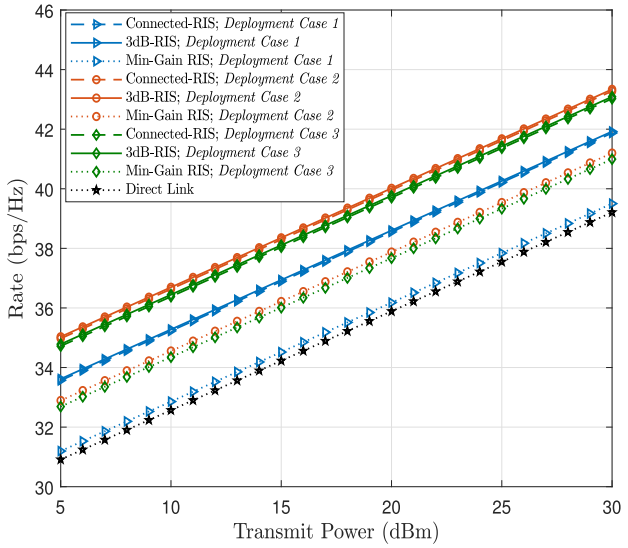

FIGURE 14. Rate versus transmit power for $\Delta G^{\text{dB}} = 3$ dB and $\phi_{\text{UE}} = 80°$.

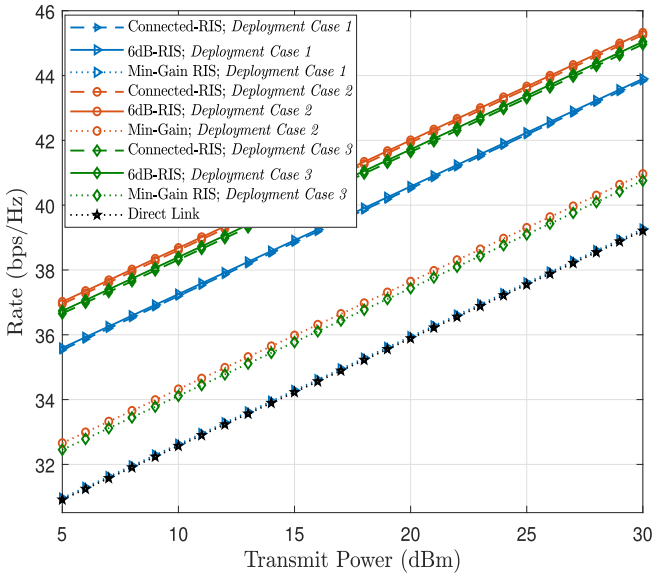

FIGURE 15. Rate versus transmit power for $\Delta G^{\text{dB}} = 6$ dB and $\phi_{\text{UE}} = 80°$.

the phase shifts of the incident signals, thereby enhancing the received signal strength at the UE. Furthermore, since all the configurations are deployed with the same resource allocation strategies, their ensuing performance remains comparable despite differences in their architectural complexity. These findings underscore a key advantage of the Connected-RIS: it offers comparable performance to the fully controlled RIS, while significantly reducing the power consumption and control overhead. As a result, the Connected-RIS emerges as a more energy-efficient and cost-effective alternative that still satisfies the quality-of-service requirements as the conventional designs.

E. RIS CONFIGURATION AND CASE STUDY

It is important to recall that the objective is to ensure fair coverage over the angular region defined by the azimuth

Algorithm 3 Computation of the Required Number of Codewords.

Input: Gain threshold G_{th}.

1: Initialize $q = 1$, $N_{\text{conf}} \leftarrow 0$, $\phi_q \leftarrow -80°$.
2: **while** $\phi_q \leq 80°$ **do**
3: Compute the RIS gain $G_{\text{RIS}}(\phi)$ for $\phi \in [-80°{:}1°{:}80°]$.
4: Identify ϕ_q such that $G_{\text{RIS}}(\phi_q) = G_{\text{th}}$.
5: Set $N_{\text{conf}} \leftarrow N_{\text{conf}} + 1$ and $q \leftarrow q + 1$.
6: **end while**

Output: Required number of configurations N_{conf}.

range $\phi = -80°$ to $\phi = 80°$ at a fixed elevation angle θ_{RIS}, while maintaining constant azimuth angle ϕ_{BS} and elevation angle θ_{BS} at the BS. To achieve the maximum gain throughout the coverage area, the RIS must be continuously reconfigured to steer its beam towards the azimuth direction ϕ, such that the resulting gain $G_{\text{RIS}}(\phi)$ meets or exceeds a predefined threshold value G_{th}. The minimum number of distinct codewords required to achieve full coverage under this criterion can be systematically determined using Algorithm 3.

1) CONFIGURATION APPROACHES

By applying Algorithm 3, the number of codewords required to achieve full coverage is determined when using the Connected-RIS or the fully controlled RIS designs. For instance, to span the angular range from $-80°$ to $80°$, the 83×83 Connected-RIS requires only 52 codewords, whereas the min-gain RIS necessitates 80 codewords. Based on this analysis, two deployment strategies can be considered. In the first scenario, the RIS is dynamically reconfigured using a register that stores all predefined codewords, allowing the beam to be steered in real time towards the desired direction. In the second scenario, 52 Connected-RIS panels of size 83×83 are deployed, each pre-configured with a fixed phase setting to cover a specific angular sector.

- *Dynamically Configured Surface:* In this approach, a single 83×83 Connected-RIS is dynamically reconfigured using a register that stores all 52 codewords, each corresponding to a distinct beam steering direction. The FPGA sequentially activates these codewords to steer the beam as required. This configuration offers greater adaptability and occupies a significantly less physical space than the multi-panel alternative, making it well-suited for dynamic or space-constrained environments. However, it requires fast-switching circuitry to minimize potential service interruptions during the reconfiguration, which may otherwise result in coverage gaps. For instance, storing all 52 codewords requires approximately 1,075,684 bits for the fully controlled RIS with gain margin (6,889 elements $\times 3$ bits per element $\times 52$ codewords), and only 12,948 bits for the Connected-RIS (83 control units $\times 3$ bits $\times 52$

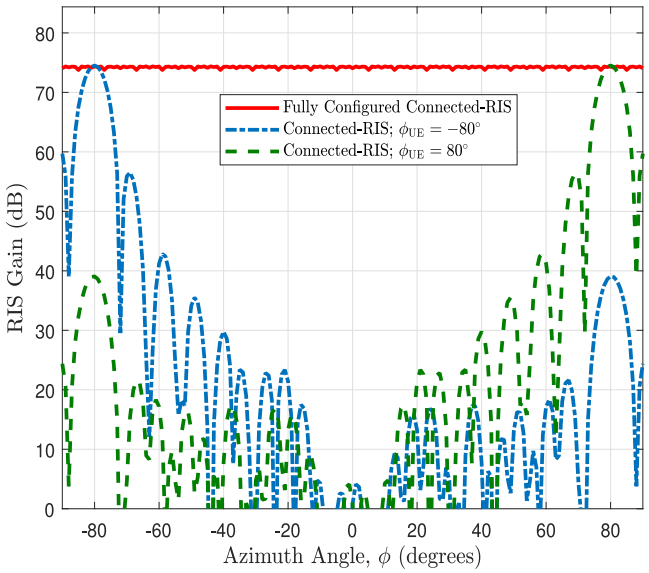

FIGURE 16. RIS gain versus the azimuth angle ϕ with multiple configurations to cover the region from $-80°$ to $80°$ in *Deployment Case 1*. Here, $\Delta G^{\text{dB}} = 6$ dB, $\psi_{\text{th}} = 31°$.

codewords). The RIS provides coverage and high signal quality for multiple users moving through the streets and inside buildings within a 160° sector. We assume that the beam selection algorithm updates every 100 ms.

- *Static Configured Surface:* In this configuration, 52 individual 83 × 83 Connected-RIS panels are deployed, each pre-configured with a fixed phase setting tailored to a specific angular sector. This eliminates the need for dynamic reconfiguration and the associated switching delays, enabling simultaneous coverage of all target directions and significantly simplifying the control circuitry. This advantage comes at the cost of increased physical deployment space and reduced adaptability to dynamic environments. This approach is well-suited for wide-area, high-density scenarios, such as dense urban corridors, transportation hubs, smart-city deployments with largely static devices, industrial or campus environments with stable coverage zones, and peak-hour hotspots, where uninterrupted multi-sector coverage is required. In such settings, the static panels continuously enhance the signal within their assigned sectors, ensuring robust and consistent connectivity for both user-centric and machine-type communications.

For both configuration approaches, the RIS gain performance is illustrated in Fig. 16 for representative steering angles ($\phi_{\text{UE}} = -80°$ and $\phi_{\text{UE}} = 80°$).[12] The results indicate that the main lobes exhibit high gains, approaching 76 dB, while the side lobes remain significantly attenuated. By continuously configuring the RIS, full coverage of the said region can be obtained. This multi-beam strategy underscores the flexibility and efficiency of the Connected-RIS design in achieving wide-area coverage with reduced hardware complexity.

[12]The same behavior is observed when the gain margin is $\Delta G^{\text{dB}} = 3$ dB or when considering the other deployment cases (*Case 2* and *Case 3*). To reduce the number of figures, we present only the illustrative result shown in Fig. 16.

2) POWER CONSUMPTION EVALUATION

In this subsection, the power consumption of the dynamically configured surface and the static configured surface is discussed.

- *Dynamically Configured Surface:* For this setup, the total power consumption is influenced by multiple factors, including the RIS size, the configuration update rate, the type of switching elements, and the complexity of the control circuitry. Following the model in [12], we assume a power requirement of 300 mW per configuration update for the updating circuitry. Accordingly, the total power consumption of the Connected-RIS (83 × 83) is estimated at approximately 314.64 W, significantly lower than the 5628.78 W required by the fully controlled RIS with gain margin (6dB-RIS). For further comparison, the fully controlled RIS with minimum gain (min-gain RIS) under the same deployment conditions consumes about 2278.68 W. These findings underscore the energy efficiency of the Connected-RIS architecture, which achieves a substantial power reduction of 94.4% and 86.20% relative to the 6dB-RIS and the min-gain RIS designs, respectively. This highlights the practical viability of the Connected-RIS in energy-constrained environments, particularly for large-scale or real-time applications.
- *Static Configured Surface:* Here, the power consumption remains relatively stable over time but is distributed across multiple panels, with the total power determined by the cumulative consumption of each individual panel. For this setup, the total power consumption is estimated to be approximately 314.34 W for the Connected-RIS (83 × 83), compared to 5628.48 W for the 6dB-RIS and 2278.38 W for the min-gain RIS. Consistent with the dynamic configuration scenario, the Connected-RIS exhibits lower power consumption compared to the benchmark designs, reaffirming its suitability for scalable and power-sensitive deployments.

VI. CONCLUSION

This work introduced and validated a correlation-based RIS architecture, termed Connected-RIS, which effectively addresses the dual challenges of hardware simplification and energy consumption reduction in emerging RIS-aided wireless communication systems. By exploiting the correlation among the phase shifts values of the RIS, which is analyzed and confirmed for different deployments, the proposed design substantially reduces the number of independently controlled components, thereby minimizing the control signal requirements and simplifying the associated circuitry. Theoretical evaluations and extensive simulations across diverse deployment scenarios demonstrated that the Connected-RIS achieves significant reductions in

both, the power consumption and the hardware complexity, while maintaining competitive beamforming gains and data rates. In comparison to the fully controlled RIS designs, the Connected-RIS offers a favorable balance between system performance and implementation cost, representing a critical advancement towards scalable and energy-aware RIS-enabled network architectures.

REFERENCES

[1] W. Chen et al., "5G-advanced toward 6G: Past, present, and future," *IEEE J. Sel. Areas Commun.*, vol. 41, no. 6, pp. 1592–1619, Jun. 2023.

[2] J. Zhang, R. Xiong, J. Liu, T. Mi, and R. C. Qiu, "Design and prototyping of transmissive RIS-aided wireless communication," 2024, *arXiv:2402.05570*.

[3] M. Alsabah et al., "6G wireless communications networks: A comprehensive survey," *IEEE Access*, vol. 9, pp. 148191–148243, 2021.

[4] Q. Wu and R. Zhang, "Towards smart and reconfigurable environment: Intelligent reflecting surface aided wireless network," *IEEE Commun. Mag.*, vol. 58, no. 1, pp. 106–112, Jan. 2020.

[5] X. Pei et al., "RIS-aided wireless communications: Prototyping, adaptive beamforming, and indoor/outdoor field trials," *IEEE Trans. Commun.*, vol. 69, no. 12, pp. 8627–8640, Dec. 2021.

[6] Q. Li, M. El-Hajjar, K. Cao, C. Xu, H. Haas, and L. Hanzo, "Holographic metasurface-based beamforming for multi-altitude LEO satellite networks," *IEEE Trans. Wireless Commun.*, vol. 24, no. 4, pp. 3103–3116, Apr. 2025.

[7] Q. Li, M. El-Hajjar, Y. Sun, and L. Hanzo, "Performance analysis of reconfigurable holographic surfaces in the near-field scenario of cell-free networks under hardware impairments," *IEEE Trans. Wireless Commun.*, vol. 23, no. 9, pp. 11972–11984, Sep. 2024.

[8] C. Huang, R. Mo, and C. Yuen, "Reconfigurable intelligent surface assisted multiuser MISO systems exploiting deep reinforcement learning," *IEEE J. Sel. Areas Commun.*, vol. 38, no. 8, pp. 1839–1850, Aug. 2020.

[9] Z. Mohamed and S. Aïssa, "Leveraging UAVs with intelligent reflecting surfaces for energy-efficient communications with cell-edge users," in *Proc. IEEE Int. Conf. Commun. (ICC)*, 2020, pp. 1–6.

[10] J.-B. Gros, V. Popov, M. A. Odit, V. Lenets, and G. Lerosey, "A reconfigurable intelligent surface at mmWave based on a binary phase tunable metasurface," *IEEE Open J. Commun. Soc.*, vol. 2, pp. 1055–1064, 2021.

[11] A. Rafique, A. Mehmood, N. U. Hassan, M. Q. Mehmood, and M. Zubair, "Power consumption analysis of a reconfigurable intelligent surface for self-sustained operations," in *Proc. IEEE 99th Veh. Techno. Conf. (VTC)*, 2024, pp. 1–5.

[12] Z. Li, J. Zhang, J. Zhu, and L. Dai, "RIS energy efficiency optimization with practical power models," in *Proc. Int. Wireless Commun. Mobile Comput. (IWCMC)*, 2023, pp. 1172–1177.

[13] L. Dai et al., "Reconfigurable intelligent surface-based wireless communications: Antenna design, prototyping, and experimental results," *IEEE Access*, vol. 8, pp. 45913–45923, 2020.

[14] F. Saggese, V. Croisfelt, R. Kotaba, K. Stylianopoulos, G. C. Alexandropoulos, and P. Popovski, "On the impact of control signaling in RIS-empowered wireless communications," *IEEE Open J. Commun. Soc.*, vol. 5, pp. 4383–4399, 2024.

[15] A. Rafique et al., "Reconfigurable intelligent surfaces: Interplay of unit cell and surface-level design and performance under quantifiable benchmarks," *IEEE Open J. Commun. Soc.*, vol. 4, pp. 1583–1599, 2023.

[16] A. Enqvist, Ö. T. Demir, C. Cavdar, and E. Björnson, "Control signaling for reconfigurable intelligent surfaces: How many bits are needed?" in *Proc. IEEE Int. Conf. Commun. (ICC)*, 2025, pp. 6856–6861.

[17] E. Koutsonas, X. Mu, N. Qi, S. Trevlakis, T. A. Tsiftsis, and A.-A. A. Boulogeorgos, "Simultaneous information and control signalling protocol for RIS-empowered wireless systems," 2025, *arXiv:2508.04185*.

[18] X. Zhou, T. Fang, Y. Mao, and B. Clerckx, "Generalized beyond-diagonal RIS architectures: Theory and design via structure-oriented symmetric unitary projection," 2025, *arXiv:2509.17804*.

[19] Q. Li, M. El-Hajjar, I. Hemadeh, A. Shojaeifard, and L. Hanzo,"Coordinated reconfigurable intelligent surfaces: Non-diagonal group-connected design," *IEEE Trans. Veh. Technol.*, vol. 73, no. 7, pp. 10811–10816, Jul. 2024.

[20] X. Zhou, T. Fang, and Y. Mao, "A novel Q-stem connected architecture for beyond-diagonal reconfigurable intelligent surfaces," in *Proc. IEEE Int. Conf. Commun. (ICC)*, 2025, pp. 6880–6885.

[21] K. Liu, Z. Zhang, L. Dai, S. Xu, and F. Yang, "Active reconfigurable intelligent surface: Fully-connected or sub-connected?" *IEEE Commun. Lett.*, vol. 26, no. 1, pp. 167–171, Jan. 2022.

[22] *5G: System Architecture for the 5G System, Release 15, Version 15.3.0*, 3GPP Standard TS 23.501, 2018.

[23] "5G: Study on channel model for frequencies from 0.5 to 100 GHz; (Release 14), Version 14.3.0," 3GPP, Sophia Antipolis, France, Rep. TR 38.901, ETSI TR 138 901, 2018.

[24] N. Estakhri and A. Alù, "Wave-front transformation with gradient metasurfaces," *Phys. Rev. X*, vol. 6, Oct. 2016, Art. no. 41008.

[25] K. Wang, C. T. Lam, and B. K. Ng, "RIS-assisted high-speed communications with time-varying distance-dependent Rician channels," *Appl. Sci.*, vol. 12, no. 22, 2022, Art. no. 11857.

[26] Z. Mohamed and S. Aïssa, "Energy-efficient joint broadcast-unicast communications via dual-polarized aerial RIS," *IEEE Trans. Wireless Commun.*, vol. 22, no. 3, pp. 2113–2126, Mar. 2023.

[27] M. Toeltsch, J. Laurila, K. Kalliola, A. F. Molisch, P. Vainikainen, and E. Bonek, "Statistical characterization of urban spatial radio channels," *IEEE J. Sel. Areas Commun.*, vol. 20, no. 3, pp. 539–549, Apr. 2002.

[28] R. Zhang, X. Lu, J. Zhao, L. Cai, and J. Wang, "Measurement and modeling of angular spreads of three-dimensional urban street radio channels," *IEEE Trans. Veh. Technol.*, vol. 66, no. 5, pp. 3555–3570, May 2017.

[29] L. Wei, C. Huang, G. C. Alexandropoulos, C. Yuen, Z. Zhang, and M. Debbah, "Channel estimation for RIS-empowered multi-user MISO wireless communications," *IEEE Trans. Commun.*, vol. 69, no. 6, pp. 4144–4157, Jun. 2021.

[30] E. Basar, M. Di Renzo, J. De Rosny, M. Debbah, M.-S. Alouini, and R. Zhang, "Wireless communications through reconfigurable intelligent surfaces," *IEEE Access*, vol. 7, pp. 116753–116773, 2019.

[31] J. Wang, W. Tang, S. Jin, X. Li, and M. Matthaiou, "Static power consumption modeling and measurement of reconfigurable intelligent surfaces," in *Proc. Eur. Signal Process. Conf. (EUSIPCO)*, 2023, pp. 890–894.

[32] J. Wang et al., "Reconfigurable intelligent surface: Power consumption modeling and practical measurement validation," *IEEE Trans. Commun.*, vol. 72, no. 9, pp. 5720–5734, Sep. 2024.

ZINA MOHAMED (Member, IEEE) received the bachelor's degree in electrical engineering from the National Engineering School of Sfax, Tunisia, in 2017, the master's degree in embedded systems from the National Engineering School of Sfax, Tunisia, in cooperation with the Technische Universität Chemnitz, Germany, in 2017, and the Ph.D. degree in telecommunications from the Institut National de la Recherche Scientifique (INRS), Montreal, QC, Canada, in 2023. She subsequently held a postdoctoral research fellowship at the LTCC@ETS Laboratory, École de Technologie Supérieure (ETS), Montreal, Canada, from 2023 to 2024, and is currently a Postdoctoral Research Fellow at INRS, Canada.

Her research interests include reconfigurable intelligent surfaces, wireless power transfer, energy efficiency, optimization, and UAV communications. In these areas, she has published in reputed journals and conferences of the IEEE. She is recipient of the INRS-Tunisia Ph.D. Scholarship, and a co-recipient of the 2021 International Wireless Communications and Mobile Computing Conference Best Paper Award.

AMMAR B. KOUKI (Senior Member, IEEE) received the B.S. (Hons.) and M.S. degrees in Engineering Science from Pennsylvania State University, in 1985 and 1987, respectively, and the Ph.D. degree in electrical engineering from the University of Illinois at UrbanaâĂŞChampaign in 1991. He is currently a Full Professor of Electrical Engineering and the Founding Director of the LTCC@ETS Laboratory at École de Technologie Supérieure (ETS), Montreal, Canada. His research interests are in the areas of modeling, simulation and design of active and passive microwave and mm-wave devices, circuits and antennas with focus on reconfigurability and energy-efficiency. He has extensive collaboration with industry in Canada and has successfully completed multiple technology transfers to companies. His research work has led directly to the creation of multiple start-ups (EMWorks Inc., ISR Technologies and AmpliX Inc.) and has netted over 300 publications as well as 8 granted patents. Dr. Kouki is a co-founder and the current president of the non-profit North American Tunisian Engineering Group (NATEG).

SONIA AÏSSA (Fellow, IEEE) received her Ph.D. degree in Electrical and Computer Engineering from McGill University, Montreal, QC, Canada, in 1998. Since then, she has been with the Institut National de la Recherche Scientifique (INRS), Montreal, QC, Canada, where she is Cyrille-Duquet Chair Professor. During her career in telecommunications, she has held various research posts in Canada, Japan, Malaysia, Turkey, and the UK. Her research interests include the modeling, design, performance analysis and optimization of wireless systems and networks. Prof. Aïssa is Fellow of the IEEE and Fellow of the Canadian Academy of Engineering. Her awards include the NSERC University Faculty Award 1999; the Quebec Government FRQNT Strategic Faculty Fellowship 2001-2006; the INRS Performance Award multiple times, for outstanding achievements in research, teaching and outreach; the 2007 FRQNT-SYTACom Technical Community Service Award; the 2021 IEEE WICE Outstanding Achievement Award, and the 2022 IEEE VTS Women's Distinguished Career Award. She is recipient of multiple IEEE Best Paper Awards and of the 2012 IEICE Best Paper Award; and recipient of NSERC Discovery Accelerator Supplement Award. She was a Distinguished Lecturer of the IEEE Communications Society (ComSoc) 2013-2016. Prof. Aïssa was a Member-At-Large of ComSoc's Board of Governors 2014-2016. Her editorial activities include: Editorial Board Member, IEEE ACCESS 2022-2024; Editor-At-Large, IEEE TRANSACTIONS ON COMMUNICATIONS 2020-2023; Area Editor, IEEE TRANSACTIONS ON WIRELESS COMMUNICATIONS 2014-2019; Editor, IEEE TRANSACTIONS ON WIRELESS COMMUNICATIONS 2004-2012; Technical Editor, IEEE COMMUNICATIONS MAGAZINE 2004-2015; and Technical Editor, IEEE WIRELESS COMMUNICATIONS MAGAZINE 2006-2010. She has been involved in organizing many flagship conferences of the IEEE, including the 2021 IEEE International Conference on Communications for which she served as the TPC Chair. She is active in promoting women in engineering and is the Founder of the IEEE Women in Engineering Affinity Group in Montreal. She is a Member-at-Large of the ComSoc's Board of Governors 2023-2025.